A Partial Sulfuration Strategy Derived Multi-Yolk–Shell Structure for Ultra-Stable K/Na/Li-ion Storage

Xiuling Shi, Yanmei Gan, Qixin Zhang, Chaoying Wang, Yi Zhao,* Lunhui Guan,* and Wei Huang*

Metal sulfides are attractive anodes for alkali metal ion batteries due to the high theoretical capacity, while their practical implementation is hampered by the inherent poor conductivity and vast volume variation during cycles. Approaching rational designed microstructures with good stability and fast charge transfer is of great importance in response to these issues. Herein, a partial sulfuration strategy for the rational construction of multi-yolk–shell (m-Y–S) structures, from which multiple $Fe_{1-x}S$ nanoparticles are confined within hollow carbon nanosheet with tunable interior void space is reported. As anode materials, the m-Y–S $Fe_{1-x}S$@C composite can display high capacity and excellent rate capability (134, 365, and 447 mA h g^{-1} for K$^+$, Na$^+$, and Li$^+$ storage at 20 A g^{-1}). Remarkably, it exhibits ultra-stable potassium storage up to 1200, 6000, and 20 000 cycles under current densities of 0.1, 0.5, and 1 A g^{-1}, which is much superior to previous yolk–shell structures and metal-sulfide anodes. Based on comprehensive experimental analysis and theoretical calculations, the exceptional performance of m-Y–S structure can be ascribed to the optimized interior void space for good structure stability, as well as the multiple connection points and conductive carbon layer for superior electron/ion transportation.

1. Introduction

Lithium-ion batteries (LIBs) as dominant rechargeable batteries have been extensively applied for portable electronics and electrical vehicles in the past three decades, owing to its long service life as well as high energy and power density. However, the development of LIBs for large-scale energy storage systems, such as smart grids powered by intermittent solar/wind energy sources, is restricted by the scarcity, high cost, and uneven distribution of lithium resources.[1–3] Recently, increasing efforts have been devoted to Na/K-ion batteries as promising alternatives to LIBs, due to their similar electrochemical properties to that of LIBs, and the high abundance of sodium and potassium resources with low cost.[4–7] Nevertheless, the large ionic radius of Na$^+$ (1.02 Å) and K$^+$ (1.38 Å) not only causes inferior ion diffusion kinetics but also brings out serious volume variation of active materials during discharge/charge processes, thus resulting in low rate capability and poor cyclic stability. Therefore, it is very critical to develop high-performance electrode materials for the practical applications of sodium-ion batteries (SIBs) and potassium-ion batteries (PIBs).[8–10]

With respect to anode materials, metal sulfides with high capacity and excellent redox reversibility have been identified as promising anode candidates for efficient Na/K-ion storage.[11–14] In particular, iron sulfides (e.g., FeS$_2$, FeS, Fe$_{1-x}$S) have drawn prominent attention owing to the high theoretical capacity (e.g., 894 mA h g^{-1} for FeS$_2$), low cost, natural abundance, and environmental benign.[15–17] However, their inherent limitations such as poor electrical conductivity, large volume variation, and the dissolution of discharge products into electrolyte, would result in inferior rate and severe capacity fading of metal sulfide anodes during cycles. To circumvent these issues, various strategies including nanostructure design, carbon modification, heteroatom doping, voltage cut-off, and electrolyte optimization have been developed.[18–20] Among them, the combination of metal sulfide and carbon nanomaterials has been confirmed as a valid strategy, which can effectively improve the conductivity and buffers the volume changes of metal sulfides during cycles.[21–24] Thus, a series of iron sulfide/carbon composites with tailored structures (e.g., Fe$_{1-x}$S@C, FeS$_2$@C, FeS$_2$/graphene, Fe$_{1-x}$S@carbon nanotube) have been synthesized for good battery performance.[25–31]

X. L. Shi, Y. M. Gan, Q. X. Zhang, C. Y. Wang, Prof. Y. Zhao,
Prof. W. Huang
Fujian Cross Strait Institute of Flexible Electronics (Future Technologies)
Fujian Normal University
Fuzhou 350117, China
E-mail: zhaoyi@fjnu.edu.cn; provost@nwpu.edu.cn
X. L. Shi, Y. M. Gan, Prof. L. H. Guan
CAS Key Laboratory of Design and Assembly of Functional
Nanostructures
Fujian Key Laboratory of Nanomaterials
Fujian Institute of Research on the Structure of Matter
Chinese Academy of Sciences
Fuzhou 350108, China
E-mail: guanlh@fjirsm.ac.cn
Prof. W. Huang
Frontiers Science Center for Flexible Electronics (FSCFE)
MIIT Key Laboratory of Flexible Electronics (KLoFE)
Northwestern Polytechnical University
Xi'an 710072, China
Prof. W. Huang
Key Laboratory of Flexible Electronics (KLOFE) & Institute of Advanced
Materials (IAM)
Nanjing Tech University (NanjingTech)
Nanjing 211800, China

**ADVANCED
SCIENCE NEWS**

www.advancedsciencenews.com

**ADVANCED
MATERIALS**

www.advmat.de

Especially, yolk–shell (Y–S) structured composites, owing to its unique interior void space and outer protective shell, is capable of accommodating the volume variation and preventing the aggregation of active material, thus giving rise to good structure stability and superior battery performance.[32–37] For example, Y–S FeS@C nanospheres have been fabricated by Wang and co-workers through an SiO_2 hard template method.[38] As an SIB anode, it can remain a high capacity of 488 mA h g^{-1} after 300 cycles at 0.1 A g^{-1}. Unfortunately, so far reported Y–S composites usually exhibited large yolk size and point-to-point connection between yolk and shell, which hampered the fast electron/ion transportation from carbon shell to yolk and increase the charge diffusion distance within yolk. Moreover, the huge volume fluctuation of active material would disrupt the efficient connection between yolk and shell. These factors restricted the rate capacity and long cyclic life of Y–S anodes to some extent.[39–42] Consequently, it is still a great challenge to boost the charge transportation ability of Y–S structured composites for realizing high-performance anode materials.[43–46]

Herein, we report a partial sulfuration strategy for the construction of multi-yolk–shell (m-Y–S) structures, aiming to reduce the yolk size and enhance the contact points between shell and yolk for superior charge transportation. In the as-prepared samples, multiple $Fe_{1-x}S$ nanoparticles were well encapsulated into hollow carbon nanosheets accompanied with tunable interior void room. Compared with the traditional SiO_2-template or acid-etching method derived Y–S structure, this m-Y–S $Fe_{1-x}S@C$-3 composite presented superior structure advantages of multiple contact points, small particle size, optimized interior void room, and conductive carbon coating, thus giving rise to outstanding K/Na/Li-ion storage behavior. For potassium storage, it exhibited a high capacity of 418 mA h g^{-1} after 1200 cycles at 0.1 A g^{-1} and good rate capability of 187 mA h g^{-1} at 10 A g^{-1}. Remarkably, this anode realized ultra-stable cycling stability during K^+ storage up to 6000 cycles (311 mA h g^{-1}) at 0.5 A g^{-1} and 20 000 cycles (205 mA h g^{-1}) at 1 A g^{-1}, which was much superior to as-reported anodes for PIBs. As anodes for LIBs and SIBs, $Fe_{1-x}S@C$-3 anode also manifested excellent cycling retention and superior rate performance, which delivered high capacities of 633 mA h g^{-1} after 1000 cycles at 10 A g^{-1} and 321 mA h g^{-1} after 7000 cycles at 5 A g^{-1}, respectively. Moreover, theoretical calculations, kinetics analysis, and ex situ characterizations have been applied to systematically investigate the origin of superior battery performance for m-Y–S $Fe_{1-x}S@C$-3.

2. Results and Discussion

Figure 1a schematically illuminates the preparation process of m-Y–S $Fe_{1-x}S@C$ composites, which involves carbon coating, partial sulfuration, acid etching, and heat treatment. The scanning electron microscopy (SEM) and transmission electron microscopy (TEM) images in Figure 1b–m and Figure S1, Supporting Information were applied to disclose the morphology and structure of as-obtained composites. Figure 1b,c shows the hexagonal nanosheet morphology of Fe_2O_3 precursor with a thickness of 15–30 nm and a width of 200–300 nm.[47] The

interlayer spacing of 0.251 nm in Figure 1d was attributed to the (110) plane of Fe_2O_3. Subsequently, a carbon layer was uniformly applied through the carbonization treatment of the resorcinol-formaldehyde resin coating on Fe_2O_3 nanosheets.[48] Figure 1e,f and Figure S1d–f, Supporting Information exhibit the core–shell $Fe_3O_4@C$ structure with a smooth carbon shell (thickness of ≈7 nm) on Fe_3O_4 nanosheet. The high-resolution TEM (HRTEM) image in Figure 1e shows a characteristic interplanar distance of 0.253 nm, assigning to the (311) plane of Fe_3O_4 phase. Then, $Fe_3O_4@C$ composite was partially vulcanized with certain amount of sulfur to generate $Fe_3O_4/FeS_2@C$ composite. Seen from Figure 1h,i, the morphology remained unchanged after partial sulfuration. While, Figure 1j showed the interlayer spacings of 0.253 and 0.270 nm, which matched well with the (311) plane of Fe_3O_4 and (200) plane of FeS_2, respectively. Finally, the m-Y–S structure was realized based on the different chemical reactivity between metal oxide and metal sulfide. The m-Y–S $Fe_{1-x}S@C$ composite can be achieved through the facile etching of Fe_3O_4 with HF solution and subsequent annealing treatment. As confirmed in Figure 1k,l and Figure S1j–l, Supporting Information multiple $Fe_{1-x}S$ nanoparticles (NPs) with irregular morphology were located within hollow carbon nanosheets. There was large inner void room between carbon shell and $Fe_{1-x}S$ yolk. Figure 1m exhibits the regular interplanar spacing of 0.207 nm, which can be attributed to the (2022) plane of $Fe_{1-x}S$ phase. The crystal structures of Fe_2O_3, Fe_3O_4, FeS_2, and $Fe_{1-x}S$ phases can be further confirmed by the fast Fourier transform (FFT) images in Figure S1, Supporting Information.

The structure evolution of these composites was further evaluated through X-ray diffraction (XRD) characterization. Seen from Figure S2, Supporting Information original Fe_2O_3 nanosheets manifested characteristic peaks of rhombohedral Fe_2O_3 (JCPDS No. 33–0664), which was completely converted into cubic phase of Fe_3O_4 (JCPDS No. 19–0629) after carbon coating. The partial sulfuration process resulted in the co-existence of Fe_3O_4 and FeS_2 (JCPDS No. 42–1340) phases. All the peaks appearing in $Fe_{1-x}S@C$-3 pattern can be well ascribed to hexagonal $Fe_{1-x}S$ (JCPDS No. 29–0726). No diffraction peaks of carbon layer were detected, suggesting its amorphous property in these composites.

It is notably that the interior void room within m-Y–S structure can be adjusted by the sulfur amount during partial sulfuration process. Four kinds of $Fe_{1-x}S@C$ composites with different void space were prepared and characterized through SEM, as shown in **Figure 2**a–h. By using sufficient sulfur, $Fe_3O_4@C$ was completely vulcanized into $Fe_{1-x}S@C$-0 composite. Seen from Figure 2a,b, $Fe_{1-x}S$ particles were compactly coated with carbon layer. Only small void space was observed due to the volume changes between different phases during fabrication process. Through partial sulfuration treatment, as-produced $Fe_{1-x}S@C$-1, $Fe_{1-x}S@C$-2, and $Fe_{1-x}S@C$-3 composites (Figure 2c–h) presented typical m-Y–S structure. It was clearly observed that multiple NPs were confined within carbon nanosheet with different internal space. Decreasing the sulfur amount progressively reduced the particle size of $Fe_{1-x}S$ and therefore created more interior space room in these composites. The element mappings (Figure S3, Supporting Information) of $Fe_{1-x}S@C$-3 composite disclosed that the yolks were composed
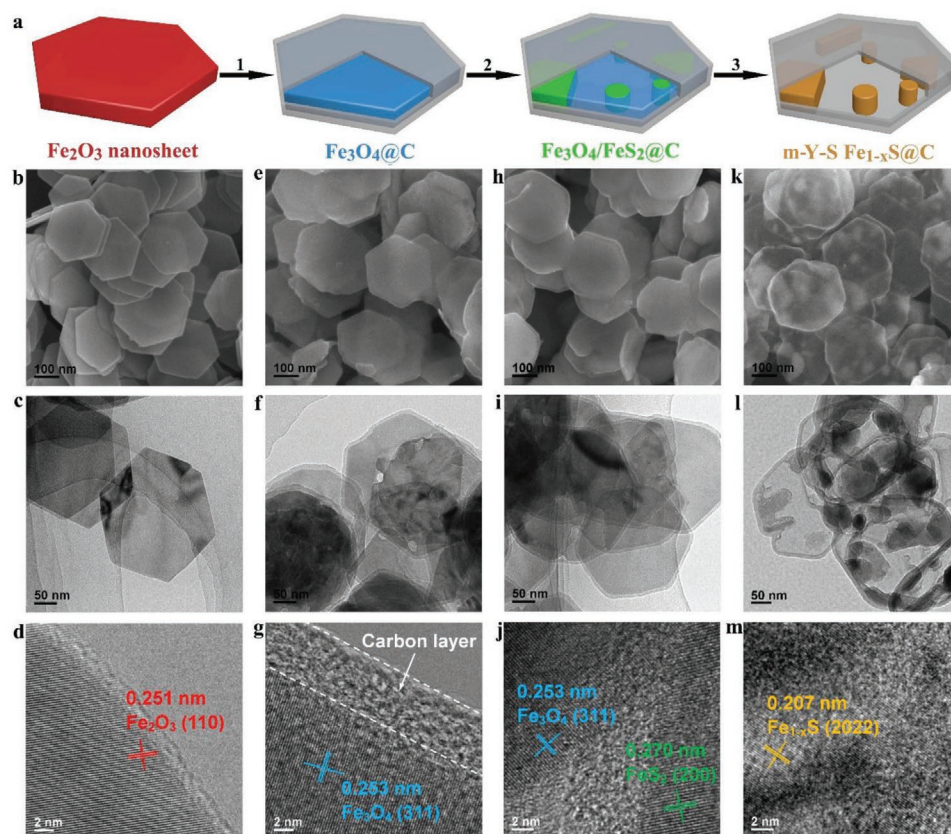
Figure 1. a) Schematic illustration for the preparation of multi-yolk–shell (m-Y–S) structures through carbon coating, partial sulfuration, and acid-etching processes. b,e,h,k) SEM, c,f,i,l) TEM, and d,g,j,m) HRTEM images of (b–d) Fe_2O_3 nanosheets, (e–g) Fe_3O_4@C, (h–j) Fe_3O_4/FeS_2@C, and (k–m) m-Y–S Fe_{1-x}S@C-3 composites.

of iron and sulfur elements, further illustrating the well encapsulation of Fe_{1-x}S yolks within carbon shell. Compared with the as-reported Y–S structures with single yolk, such m-Y–S structure can provide multiple connection points between shell and yolk for fast charge transportation, which will be further discussed below. Pure Fe_{1-x}S was also synthesized through the direct sulfuration treatment of Fe_2O_3 nanosheet. The SEM images in Figure S4, Supporting Information exhibit the irregular morphology of Fe_{1-x}S with large particle size up to several hundred nanometers.

Figure S5, Supporting Information displays the XRD patterns of m-Y–S Fe_{1-x}S@C composites, which present the characteristic diffraction peaks of Fe_{1-x}S phase. No impurity peaks were detected, verifying the high purity of these composites. The diffraction peaks were gradually weaker and broader from Fe_{1-x}S@C-0 to Fe_{1-x}S@C-3, coinciding with the decrease of particle size from SEM observations. The weight contents of Fe_{1-x}S in these composites were determined through thermogravimetry analyses (TGA) in Figure 2i. Seen from Figure S4d, Supporting Information bare Fe_{1-x}S was calcinated in air to form Fe_2O_3 with a weight loss of 14 wt%, deducing that the x value was about 0.13.[45] Therefore, the loading ratios of Fe_{1-x}S can be calculated to be 91, 78, 64, and 48 wt% for Fe_{1-x}S@C-0, Fe_{1-x}S@C-1, Fe_{1-x}S@C-2, and Fe_{1-x}S@C-3, respectively. The porosity properties of these Fe_{1-x}S@C composites were further studied by N_2 adsorption–desorption measurement in

Figure 2j,k. During partial sulfuration process, decreasing the weight ratio between sulfur and Fe_3O_4@C can lead to an increase of surface area and total pore volume. The surface area of Fe_{1-x}S@C-0 increased from 56 to 134, 250, and 382 m^2 g^{-1} for Fe_{1-x}S@C-1, Fe_{1-x}S@C-2, and Fe_{1-x}S@C-3, respectively. The pore size distribution in Figure 2k was obtained through desorption isotherm by using Barrett–Joyner–Halenda (BJH) model. It can be seen that the pore size of m-Y–S structured composites mainly concentrated at mesopores of 2.0, 4.0, and 12.3 nm. With a decreasing Fe_{1-x}S content, the amount of mesopores gradually increased, leading to the increasement of total pore volume from 0.38 cm^3 g^{-1} for Fe_{1-x}S@C-1 to 1.06 cm^3 g^{-1} for Fe_{1-x}S@C-3, consistence with the SEM images in Figure 2. X-ray photoelectron spectroscopy (XPS) was also conducted to explore the surface chemical composition of Fe_{1-x}S@C-3 composite. As expected, the existence of C, S, and Fe elements was confirmed in the survey spectrum (Figure S6a, Supporting Information). The high-resolution C 1s spectrum in Figure S6b, Supporting Information can be deconvoluted into three peaks at 284.8, 286.1, and 288.9 eV, which were assigned to the C–C, C–S/C–O, and O-C = O, respectively.[49] In Figure S6c, Supporting Information S 2p spectrum contained four typical peaks for S^{2-} (161.6 and 162.7 eV) and S_n^{2-} (164.0 and 165.1 eV).[50,51] The latter two peaks exhibited higher intensity than the former two. Thus, these two peaks at 164.0 and 165.1 eV also included the S $2p_{3/2}$ and S $2p_{1/2}$ of thiophene-type
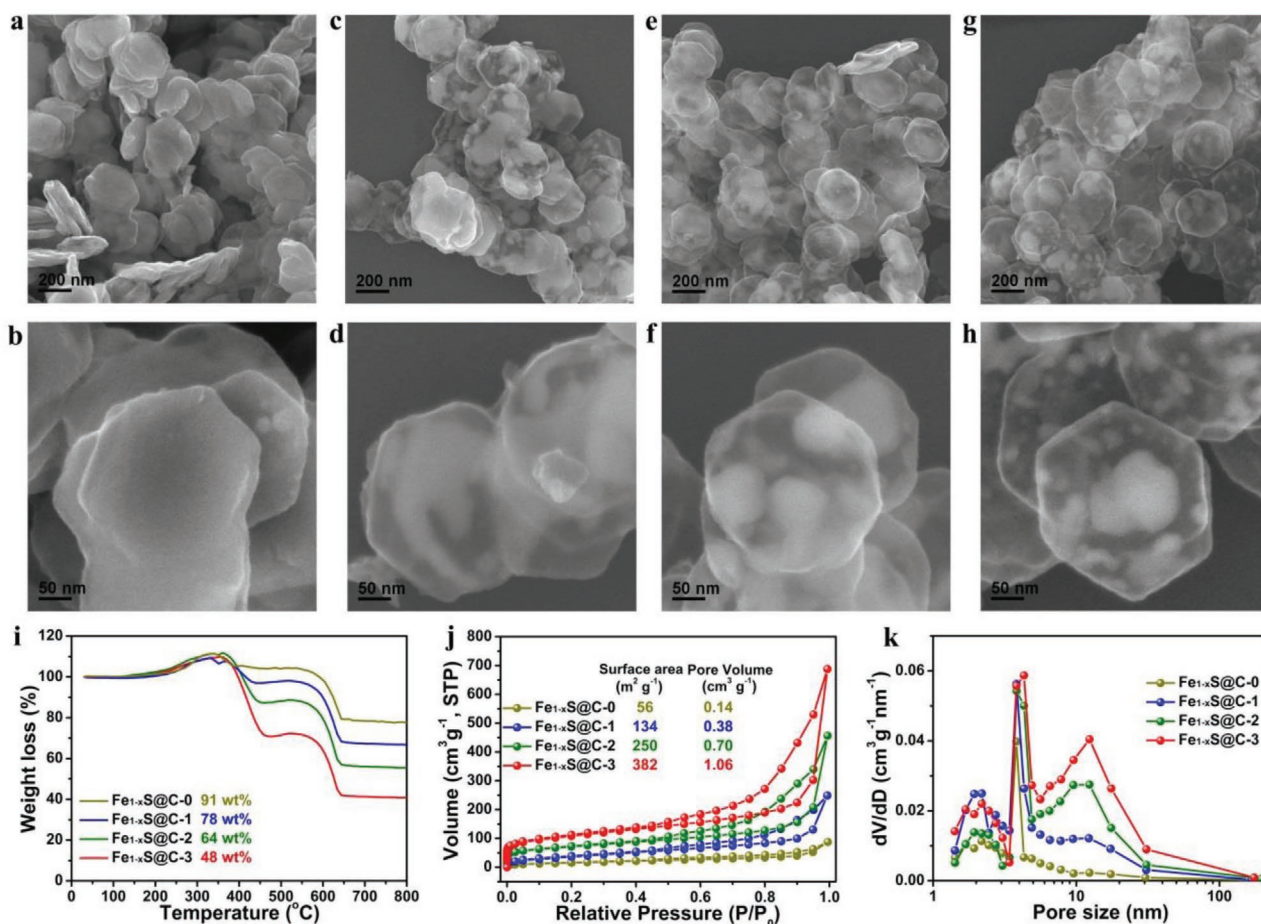
**ADVANCED
SCIENCE NEWS**
www.advancedsciencenews.com

**ADVANCED
MATERIALS**
www.advmat.de

Figure 2. SEM images of a,b) $Fe_{1-x}S@C-0$, c,d) $Fe_{1-x}S@C-1$, e,f) $Fe_{1-x}S@C-2$, and g,h) $Fe_{1-x}S@C-3$ composites. i) TGA curves, j) nitrogen adsorption–desorption isotherms, and k) pore size distribution profiles of m-Y–S $Fe_{1-x}S@C$ composites with tunable void space.

sulfur, indicating the S doping within carbon layer.[45] The other two peaks (167.1 and 168.7 eV) were related to oxidized-type SO_x. For Fe 2p spectrum, it presented characteristic peaks for Fe^{2+} (711.1 and 724.5 eV), Fe^{3+} (714.3 and 727.5 eV), and metallic Fe (707.7 eV).[27] However, the intensity of these peaks was rather weak, implying that $Fe_{1-x}S$ NPs were fully covered with carbon layer.

A series of electrochemical tests were conducted to evaluate the performance of $Fe_{1-x}S@C$ composites as PIB anodes. **Figure 3**a displays the typical cyclic voltammetry (CV) curves of $Fe_{1-x}S@C-3$ electrode at 0.2 mV s^{-1} between 0.05 and 2.8 V. During the initial cathodic process, there were two peaks around 0.72 and 0.37 V. The pronounced cathodic peak at 0.72 V could be ascribed to the potassiation process to generate K-rich phase ($K_yFe_{1-x}S$).[45] Since the peak intensity was significantly decreased in the subsequent cycles, this peak also included the irreversible formation of solid electrolyte interface (SEI) film. The second peak located at 0.37 V was attributed to the reduction process to generate metallic Fe and K_2S. Two broad peaks were observed at 1.53 and 2.34 V in the first anodic scan, which can be attributed to the reverse conversion reaction to form $K_yFe_{1-x}S$, as well as the deintercalation process in K-rich phase, respectively.[29] To further reveal the reaction mechanism of $Fe_{1-x}S$ during K^+ storage, ex situ XRD and HRTEM tests

were carried out (Figure S7, Supporting Information). At the initial discharge state of 0.8 V, the diffraction peaks of original $Fe_{1-x}S$ were converted into K-rich phases of $KFeS_2$ and $K_9Fe_2S_7$, which was also proved in the HRTEM images (Figure S7c, Supporting Information). These phases were gradually disappeared when discharged to 0.05 V. The XRD profiles at low voltages cannot identify the peaks of Fe phase, probably resulting from the low crystalline and small size of discharged product. While, the HRTEM image at 0.05 V exhibited the interlayer distance of 0.21 nm, corresponding to the (111) plane of Fe. During the charging process, the XRD peaks of $KFeS_2$ were reappeared at various voltage states of 1C 0.8 V, 1C 1.5 V and 1C 2.8 V, and the interlayer spacing of 0.29 nm for $KFeS_2$ was confirmed at the initial fully charged sate in Figure S7e, Supporting Information. In the second cycle, the reversible disappearance/generation of $K_yFe_{1-x}S$ was observed during discharge/charge processes. These results elucidated that $Fe_{1-x}S$ anode manifested reversible intercalation/deintercalation reaction in K-rich phase as well as the conversion reaction between $K_yFe_{1-x}S$ and metallic Fe during potassiation and depotassiation cycles.[45]

Figure 3b and Figure S8, Supporting Information exhibited the selected discharge/charge profiles of as-prepared anodes at a low current density of 0.1 A g^{-1}. Based on the above TGA and BET results, the carbon contents in these composites gradually
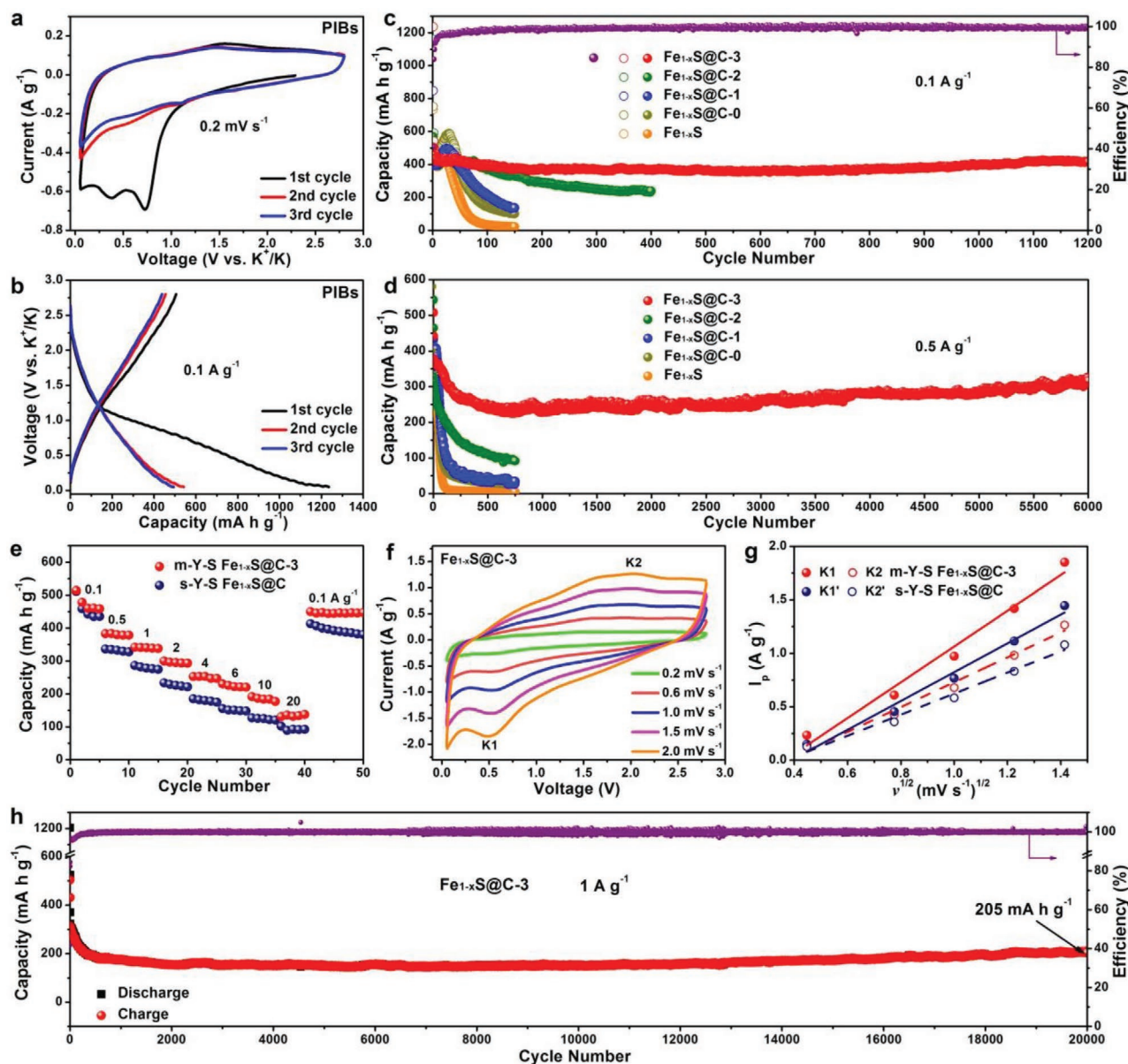
Figure 3. Potassium storage performance of m-Y–S structured composites. a) CV curves at 0.2 mV s^{-1}, and b) discharge/charge profiles at 0.1 A g^{-1} of Fe$_{1-x}$S@C-3 electrode in the initial three cycles. Cycling performance of Fe$_{1-x}$S, Fe$_{1-x}$S@C-0, Fe$_{1-x}$S@C-1, Fe$_{1-x}$S@C-2, and Fe$_{1-x}$S@C-3 electrodes at current densities of c) 0.1 A g^{-1} and d) 0.5 A g^{-1}. e) Rate capability of m-Y–S Fe$_{1-x}$S@C-3 and s-Y–S Fe$_{1-x}$S@C anodes from 0.1 to 20 A g^{-1}. f) CV curves of Fe$_{1-x}$S@C-3 under various sweep rates from 0.2 to 2.0 mV s^{-1}. g) Peak current versus $v^{1/2}$ and the corresponding linear fits of m-Y–S Fe$_{1-x}$S@C-3 and s-Y–S Fe$_{1-x}$S@C electrodes. h) Long-term cycling stability of Fe$_{1-x}$S@C-3 electrode at 1 A g^{-1}.

increased from 9 wt% for Fe$_{1-x}$S@C-0 to 52 wt% for Fe$_{1-x}$S@C-3, accompanied with an increasing interior void space from 0.14 to 1.06 cm^3 g^{-1}. As can be seen, bare Fe$_{1-x}$S, Fe$_{1-x}$S@C-0, and Fe$_{1-x}$S@C-1 electrodes with low carbon content and small pore volume delivered initial charge capacities of 423, 433, 444 mA h g^{-1}, respectively. These low capacities were due to the low electrical conductivity and large particle size of bare Fe$_{1-x}$S, as well as the squeezing of carbon shell with deficient utilization of Fe$_{1-x}$S during cycles.[52,53] The large interior void space can facilitate the utilization of active material with enhanced potassium storage capacity. Thus, the initial discharge/charge profiles of Fe$_{1-x}$S@C-2 and Fe$_{1-x}$S@C-3 electrodes delivered

capacities of 1161/569 and 1236/505 mA h g^{-1}, respectively. The irreversible capacities in the initial cycle were mainly resulted from the irreversible formation of SEI film, which were commonly observed in the nanostructured anodes for PIBs.[54–56] The cycling performance of these anodes was evaluated at a current density of 0.1 A g^{-1}. As shown in Figure 3c, bare Fe$_{1-x}$S and Fe$_{1-x}$S@C-0 anodes underwent electrochemical activation process with gradual capacity enhancement in the initial cycles. This phenomenon mainly resulted from the large volume expansion/extraction of Fe$_{1-x}$S, which led to the exposure of new fresh electrochemical reactive sites during cycles. However, this process was accompanied with the continual

**ADVANCED
SCIENCE NEWS**

www.advancedsciencenews.com

**ADVANCED
MATERIALS**

www.advmat.de

formation of SEI layer, fracturing of carbon shell, as well as severe aggregation and pulverization, thus leading to the low columbic efficiency (84–93% in Figure S8, supporting Information) and rapid capacity fading since from 30th cycle.[28,57,58] As a result, Fe$_{1-x}$S and Fe$_{1-x}$S@C-0 only maintained low capacities of 22 and 100 mA h g^{-1} after 150 cycles.

By optimizing the interior void space in m-Y–S structure, the cycling behavior can be significantly improved. The m-Y-S Fe$_{1-x}$S@C-1 delivered slightly enhanced cycling retention than Fe$_{1-x}$S@C-0. However, the small internal void room in Fe$_{1-x}$S@C-1, which was not sufficient for the volume accommodation, also resulted in the cracking of carbon shell, capacity activation process, and serious capacity decay in the following cycles.[36] After 150 cycles, it only kept a low capacity of 136 mA h g^{-1} at 0.1 A g^{-1}. For Fe$_{1-x}$S@C-2, the increasement of void space and carbon content (36 wt%) enabled excellent cycling performance in the initial cycles and sustained a high capacity of ≈400 mA h g^{-1} at 80th cycles. After that, the capacity started to decline and remained at 240 mA h g^{-1} after 400 cycles, probably due to the destruction of carbon layer after successive cycles. Among the three m-Y-S composites, Fe$_{1-x}$S@C-3 anode showed the best cyclic stability. It can maintain high capacities of 413, 386, 368, 362, and 418 mA h g^{-1} after 50, 100, 300, 500, and 1200 cycles, respectively. The columbic efficiency quickly increased up to 95% after 10 cycles and kept stable around 99% in the subsequent cycles, which was higher than the CE of other electrodes (Figure S8, Supporting Information). Moreover, the Fe$_{1-x}$S@C-3 still presented the best cycling retention among these composites at a high current density of 0.5 A g^{-1}. It can sustain a notable capacity of 311 mA h g^{-1} even after 6000 cycles. Such excellent cycling performance can be assigned to the sufficient interior void space and high carbon content of Fe$_{1-x}$S@C-3 composite for good structure stability and efficient charge transfer during cycles. In comparison, Fe$_{1-x}$S, Fe$_{1-x}$S@C-0, Fe$_{1-x}$S@C-1, and Fe$_{1-x}$S@C-2 only remained low capacities of 5, 28, 34, and 92 mA h g^{-1} at 0.5 A g^{-1} after 750 cycles, respectively.

To illuminate the structure advantage of m-Y–S composite, we compared the rate performance of Fe$_{1-x}$S@C-3 with single-yolk–shell (s-Y–S) Fe$_{1-x}$S@C. The Fe$_{1-x}$S@C composite, which was prepared through acid etching of Fe$_3$O$_4$@C followed with sulfuration treatment, exhibited typical Y–S structure with single Fe$_{1-x}$S particle encapsulated within hollow carbon layer (Figure S9, Supporting Information).[59] The TGA curve (Figure S10, Supporting Information) showed that the weight content of Fe$_{1-x}$S was around 50 wt%, indicating the similar interior pore volume between s-Y–S Fe$_{1-x}$S@C and m-Y–S Fe$_{1-x}$S@C-3 composites. As shown in Figure 3e and Figure S11, Supporting Information, the m-Y–S structure presented better rate behavior than the s-Y–S structure. Fe$_{1-x}$S@C-3 can sustain high capacities of 380, 340, 297, 253, and 225 mA h g^{-1} at 0.5, 1, 2, 4, and 6 A g^{-1}, respectively. Even at high current densities of 10 and 20 A g^{-1}, specific capacities of 187 and 134 mA h g^{-1} were still maintained. When switched back to 0.1 A g^{-1}, a stable capacity of 446 mA h g^{-1} can be obtained. On the other side, the s-Y–S Fe$_{1-x}$S@C presented inferior rate capacities of 148, 122, and 92 mA h g^{-1} at 6, 10, and 20 A g^{-1}, respectively. Besides, compared with the SiO$_2$ template-derived Y–S structure, m-Y–S Fe$_{1-x}$S@C-3 also exhibited significantly improved

rate capability and cycling performance (Table S1, supporting Information).[45]

In order to disclose the reason of such excellent rate capability, CV tests were conducted under various sweep rates (v) between 0.2 and 2.0 mV s^{-1} (Figure 3f and Figure S12, Supporting Information). Considering that Fe$_{1-x}$S@C-3 and Fe$_{1-x}$S@C anodes were prepared and measured under same conditions, the K$^+$ diffusion coefficient (D_{K+}) can be compared through simplified Randles–Sevcik equation: $i_p = a\sqrt{D}\sqrt{v}$, where i_p, v, D, and a represent the peak current, scan rate, ion diffusion coefficient, and a constant, respectively.[54,60,61] Seen from Figure 3g, the linear fit slopes of Fe$_{1-x}$S@C-3 were larger than the values of Fe$_{1-x}$S@C. Based on the above equation, the K$^+$ diffusion coefficient of m-Y–S electrode was 1.8–2.1 times as high as s-Y–S electrode. It manifested that the multiple contact points between yolk and shell were beneficial for the fast ion transportation, leading to superior rate capacity. Moreover, we further calculated the contribution ratios of pseudocapacitance ($k_2v^{1/2}$) and ionic diffusion (k_1v) in Fe$_{1-x}$S@C-3 electrode through the following equation: $i(V) = k_1v + k_2v^{1/2}$.[62–64] The capacitive ratios of Fe$_{1-x}$S@C-3 electrode increased from 57% at 0.2 mV s^{-1} to 81% at 2 mV s^{-1} in Figure S13, Supporting Information. Figure S13b, Supporting Information displays the pseudocapacitive proportion (shaded area) of the CV curve at 1.5 mV s^{-1}, from which a high capacitive contribution of 77% was observed. Therefore, the high-rate performance of m-Y–S Fe$_{1-x}$S@C-3 can be assigned to its excellent capacitance-dominated behavior, as well as the multiple connection points for fast charge transfer.

Furthermore, Figure 3h illuminates the ultra-stable cycling behavior of Fe$_{1-x}$S@C-3 electrode at 1 A g^{-1}. As can be seen, it exhibited ultra-stable cycling retention and maintained capacities of 176, 149, 151, 173, and 205 mA h g^{-1} after 1000, 5000, 10 000, 15 000, and 20 000 cycles. The average capacity fading was only 0.0017% per cycle, and the CE values kept around 99–100% during the whole cycles, illuminating its superior structure stability under ultralong cycling test. In contrast, s-Y–S Fe$_{1-x}$S@C displayed poor cyclic retention at 1 A g^{-1} and only kept a low capacity of 104 mA h g^{-1} after 800 cycles (Figure S14, Supporting Information). This outstanding cycling retention of Fe$_{1-x}$S@C-3 anode was mainly attributed to its optimized internal void space for volume accommodation without destroying the carbon layer, as well as the multiple contact points and small yolk size for efficient charge transportation ability during cycles, thus giving rise to good cycling stability with high capacities. To the best of our knowledge, such high-rate behavior and super-long cycling life in this work outperformed most reported anodes so far for PIBs (Table S2, Supporting Information).

Density functional theory (DFT) calculations were carried out to gain further insight into the superior performance of Fe$_{1-x}$S@C-3 composite. **Figure 4**a,b, displays the charge density differences of Fe$_{1-x}$S and Fe$_{1-x}$S/C systems, respectively, from which the charge accumulation (cyan parts) and charge depletion (green parts) disclosed the charge transfer from K$^+$ to the samples.[65] For Fe$_{1-x}$S/C system, the charge accumulation was observed not only between the K atom and Fe$_{1-x}$S but also between the K atom and carbon layer. It is obvious that the charge accumulation region around Fe$_{1-x}$S/C interface is
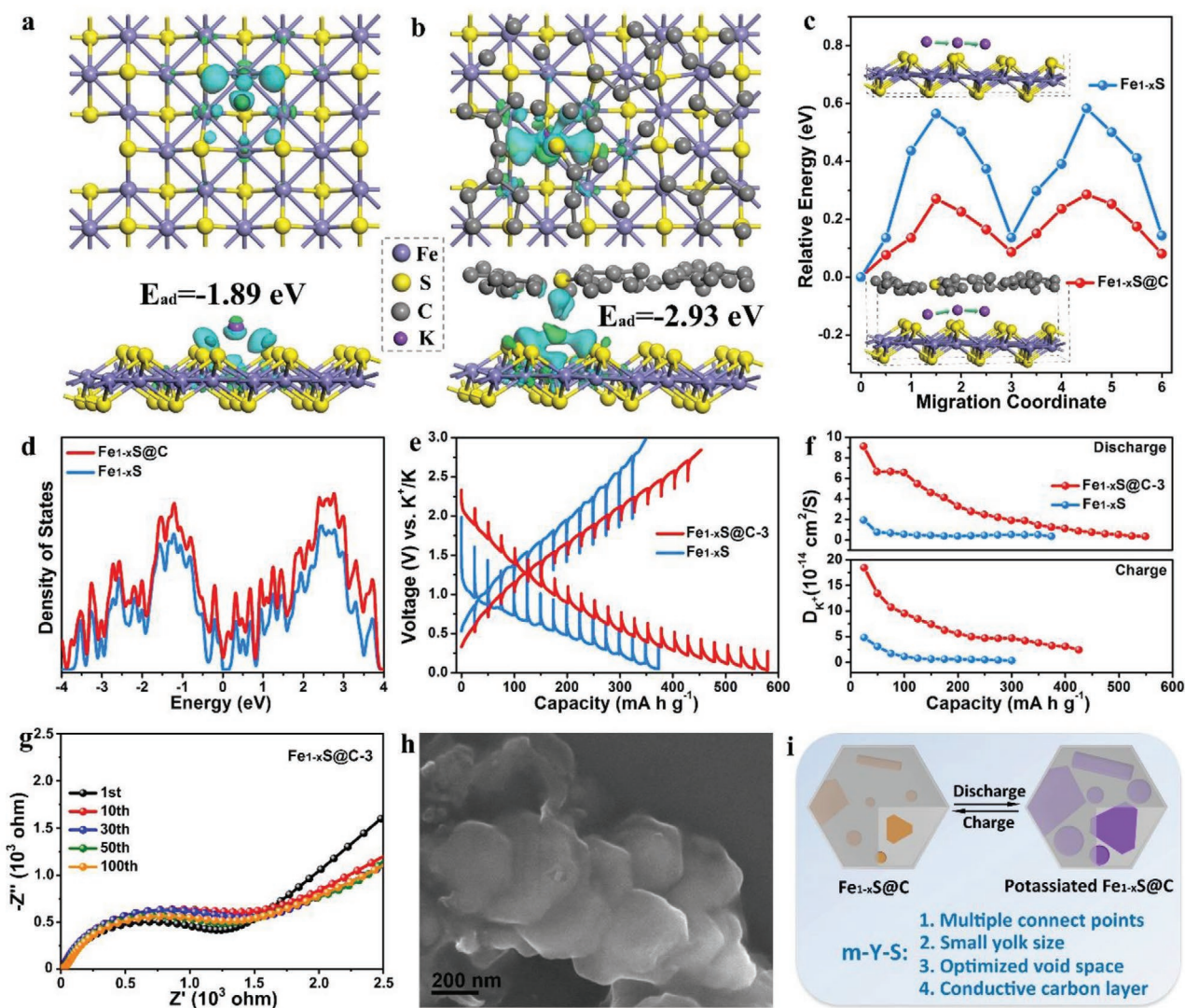
Figure 4. Charge density differences with one K-ion adsorbed for a) $Fe_{1-x}S$ and b) $Fe_{1-x}S/C$, cyan and green areas represent the charge accumulation and loss, respectively. c) K-ion migration path and diffusion energy barriers on $Fe_{1-x}S/C$ heterointerface and $Fe_{1-x}S$ surface. d) DOS for $Fe_{1-x}S$ and $Fe_{1-x}S/C$. e) GITT profiles and f) the corresponding K^+ diffusion coefficients of $Fe_{1-x}S@C-3$ and $Fe_{1-x}S$ electrodes during discharge and charge processes. Data was recorded with a series of current pulses at 50 mA g^{-1} for 30 min and 2 h relaxation at each interval. g) Nyquist impedance plots of $Fe_{1-x}S@C-3$ electrode under various cycles. h) SEM image of $Fe_{1-x}S@C-3$ electrode after 100 cycles for PIBs. i) Schematic illustration for the structure advantages of m-Y–S $Fe_{1-x}S@C-3$ composite during cycles.

larger than that of pure $Fe_{1-x}S$ surface, suggesting the strong binding energy between K^+ and $Fe_{1-x}S/C$.[66] This result was further confirmed through the adsorption energy (E_{ad}) calculation. The E_{ad} values of a single K ion on $Fe_{1-x}S$ and $Fe_{1-x}S/C$ interface (Figure S15, Supporting Information) were −1.89 and −2.93 eV, respectively. It demonstrates that the carbon coating can improve the K^+ adsorption ability of $Fe_{1-x}S$ for high ion storage capacity.[67] It is well known that the ion migration energy barrier is closely related to the electrochemical performance of PIBs.[68] Figure 4c presents the K ion diffusion path and energy barriers on these two systems by using climbing image nudged elastic band method. As can be seen, the diffusion energy barriers for $Fe_{1-x}S/C$ were much lower than those for $Fe_{1-x}S$, manifesting that carbon layer can facilitate the ion diffusion kinetics.[52,69] Lastly, the density of states (DOS)

calculation was carried out for $Fe_{1-x}S$ and $Fe_{1-x}S/C$ composites to acquire the electrical properties. Seen from the density differences at Fermi level in Figure 4d, the carbon incorporation resulted in the increase of DOS for $Fe_{1-x}S$. This indicates that the conducting $Fe_{1-x}S/C$ can display greatly enhanced electrical conductivity than the semiconducting $Fe_{1-x}S$.[70] These calculation results demonstrated that the combination of carbon layer can effectively boost the ion transport/adsorption ability and the electrical conductivity of $Fe_{1-x}S$ anode. Therefore, the rate capability of m-Y–S $Fe_{1-x}S@C$ can present much enhanced rate capabilities than pure $Fe_{1-x}S$ anode (Figure S16, Supporting Information).

The effect of carbon layer on the charge transfer kinetics of m-Y–S structure was further explored via galvanostatic intermittent titration technique (GITT) and electrochemical impedance

**ADVANCED
SCIENCE NEWS**

www.advancedsciencenews.com

**ADVANCED
MATERIALS**

www.advmat.de

spectroscopy (EIS) characterizations. Figure 4e shows the GITT profiles of Fe$_{1-x}$S@C-3 and Fe$_{1-x}$S electrodes at fifth cycle, from which different overpotentials (difference between equilibrium voltage and working voltage) can be observed under various discharge/charge states (Figure S17, Supporting Information). As can be seen, the overpotentials of Fe$_{1-x}$S@C-3 were much lower than the values of bare Fe$_{1-x}$S, indicating the superior reaction kinetics of m-Y–S composite.[71] The D_{K+} of these two electrodes can be obtained through GITT curves based on the simplified Fick's second law.[48,65] Seen from Figure 4f, the average D_{K+} of Fe$_{1-x}$S@C-3 electrode was almost 5.1–5.4 times larger than bare Fe$_{1-x}$S at discharge/charge processes. This indicates that the conductive carbon layer can significantly improve the K-ion transport kinetics of Fe$_{1-x}$S anode. EIS measurement was also conducted to explore the charge-transfer properties. The Nyquist plots of these two electrodes after 5 cycles and the fitting equivalent circuit model are shown in Figure S18, Supporting Information. Obviously, Fe$_{1-x}$S@C-3 electrode exhibited much lower charge-transfer resistance (R_{ct}) than that of bare Fe$_{1-x}$S in high–medium frequency region, suggesting the good electrical conductivity and low charge-transfer resistance of Fe$_{1-x}$S@C-3 composite.[72] The above DFT calculation, GITT and EIS tests disclosed that the carbon coating layer can effectively improve the electrical conductivity and K-ion transfer kinetics of Fe$_{1-x}$S anode, thus resulting in the high-rate capability of Fe$_{1-x}$S@C-3.

Besides, the structure evolution of m-Y–S Fe$_{1-x}$S@C-3 electrode was examined by EIS and SEM measurements. Figure 4g presented similar Nyquist plots with slightly changed charge-transfer resistance under various cycles, indicating its good structure integrity during cycles (Table S3, Supporting Information). Even after 100 cycles, the Fe$_{1-x}$S@C-3 still maintained the original nanosheet morphology (Figure 4h). As disclosed by the TEM images (Figure S19, Supporting Information), the active materials were still confined within carbon layer, demonstrating the optimized void space for excellent volume accommodation. On the other hand, Fe$_{1-x}$S@C-0 underwent severe structure destroy with broken carbon layer and aggregated particles left after 100 cycles. Therefore, we can attribute the outstanding performance of m-Y–S Fe$_{1-x}$S@C-3 to its unique structure merits in Figure 4i: 1) the m-Y–S structure can provide optimized internal space to tolerate the volume variation of Fe$_{1-x}$S; 2) the carbon layer can effectively hamper the aggregation of iron sulfide, stabilize the SEI layer, and enhance the electron/ion transfer kinetics of Fe$_{1-x}$S; 3) the large surface area and low dimension of m-Y–S structure can increase the contact area between electrolyte and electrode, benefiting for the surface capacitance effect; 4) the multiple connection points and small yolk size can increase the electron/ion transport channels and shorten the diffusion length, thus leading to fast charge transportation ability. Among these factors, the optimized void space and protective carbon coating together result in the good cycling stability. The combination of multiple yolks, small particle size, conductive carbon layer, and excellent surface capacitive behavior accounts for the superior rate performance of m-Y–S structure.

Moreover, the m-Y–S structures can be further applied as SIB and LIB anodes. **Figure 5**a–d illustrates the excellent sodium storage behavior of Fe$_{1-x}$S@C-3 composite as a SIB anode. In Figure 5a, the first discharge and charge profiles of Fe$_{1-x}$S@C-3 exhibit capacities of 1477 and 654 mA h g^{-1} at 0.2 A g^{-1}. This initial capacity loss was mainly due to the irreversible electrolyte decomposition and formation of SEI film on the electrode.[45] Figure 5b compares the cycling stability of bare Fe$_{1-x}$S, Fe$_{1-x}$S@C-0, and Fe$_{1-x}$S@C-3 at 0.2 A g^{-1}. The typical discharge/charge profiles at selected cycles were shown in Figure S20, Supporting Information. Bare Fe$_{1-x}$S anode exhibited poor cycling retention with a low capacity of 189 mA h g^{-1} after 400 cycles. For Fe$_{1-x}$S@C-0 anode, it displayed a capacity increasement and reached a high capacity of 789 mA h g^{-1} at 108th cycles. Since from 120th cycle, however, it possessed a fast capacity decline and sustained a capacity of 281 mA h g^{-1} after 400 cycles. It could be ascribed to the cracking of carbon shell and particle aggregation/pulverization after long cycles. As shown in Figure 5b, Fe$_{1-x}$S@C-3 presented significantly enhanced cycling stability than Fe$_{1-x}$S and Fe$_{1-x}$S@C-0 anodes at 0.2 A g^{-1}. It can maintain a high capacity of 451 mA h g^{-1} at 400th cycle. Figure 5c and Figure S21, Supporting Information display the rate capacities and typical discharge/charge profiles of Fe$_{1-x}$S@C-3 from 0.1 to 20 A g^{-1}, disclosing its excellent rate performance. When cycled at 0.5, 1, 2, 5, 10, 15, and 20 A g^{-1}, Fe$_{1-x}$S@C-3 can keep high specific capacities of 567, 533, 498, 457, 416, 377, and 365 mA h g^{-1}, respectively. Moreover, Fe$_{1-x}$S@C-3 exhibited excellent cyclic performance at a high rate of 5 A g^{-1} after being activated under 0.1 A g^{-1} in the initial two cycles. In Figure 5d, it showed slow capacity decay from 530 mA h g^{-1} in the third cycle to 370 mA h g^{-1} at 1000th cycle, and kept stable capacity retention in the subsequent cycles. After 7000 cycles, this electrode still maintained a high capacity of 321 mA h g^{-1}. The average capacity loss was only 0.0057% per cycle and the CE value kept around 99–100% during cycles. However, bare Fe$_{1-x}$S and Fe$_{1-x}$S@C-3 showed rapid capacity fading and retained low capacities of 29 and 46 mA h g^{-1} after 2000 cycles at 5 A g^{-1}, respectively.

The lithium storage performance of these samples was depicted in Figure 5f–j and Figure S22, Supporting Information. The initial discharge and charge capacities of Fe$_{1-x}$S@C-3 anode were 1778 and 1120 mA h g^{-1} at 0.5 A g^{-1}. It can display good cycling behavior and keep a high capacity of 983 mA h g^{-1} after 200 cycles, much higher than the values for Fe$_{1-x}$S@C-0 (221 mA h g^{-1}) and bare Fe$_{1-x}$S (215 mA h g^{-1}) anodes (Figure 5g). Even at a current density of 10 A g^{-1}, Fe$_{1-x}$S@C-3 still manifested good cycling performance with a high capacity of 633 mA h g^{-1} remained after 1000 cycles. The excellent rate performance of Fe$_{1-x}$S@C-3 was presented in Figure 5h, from which high capacities of 447, 390, and 355 mA h g^{-1} were sustained even at high rates of 20, 30 and 40 A g^{-1}, respectively. The kinetics analysis in Figure S23, Supporting Information demonstrated that the surface pseudocapacitive behavior of Fe$_{1-x}$S@C-3 electrode contributed much to its excellent rate capability for LIBs and SIBs. Besides, given that Fe$_{1-x}$S shows lower theoretical volume changes for Li$^+$ (97%) and Na$^+$ (178%) storage than the volume variation for K$^+$ storage (282%), the rate performance and volumetric capacity of m-Y–S Fe$_{1-x}$S@C for LIBs and SIBs can be further enhanced through optimizing the interior void space. The good structure stability of Fe$_{1-x}$S@C-3 composite for Li$^+$ and Na$^+$ storage was further demonstrated through the SEM images of the electrode after 100 cycles in

**ADVANCED
SCIENCE NEWS**

www.advancedsciencenews.com

**ADVANCED
MATERIALS**

www.advmat.de

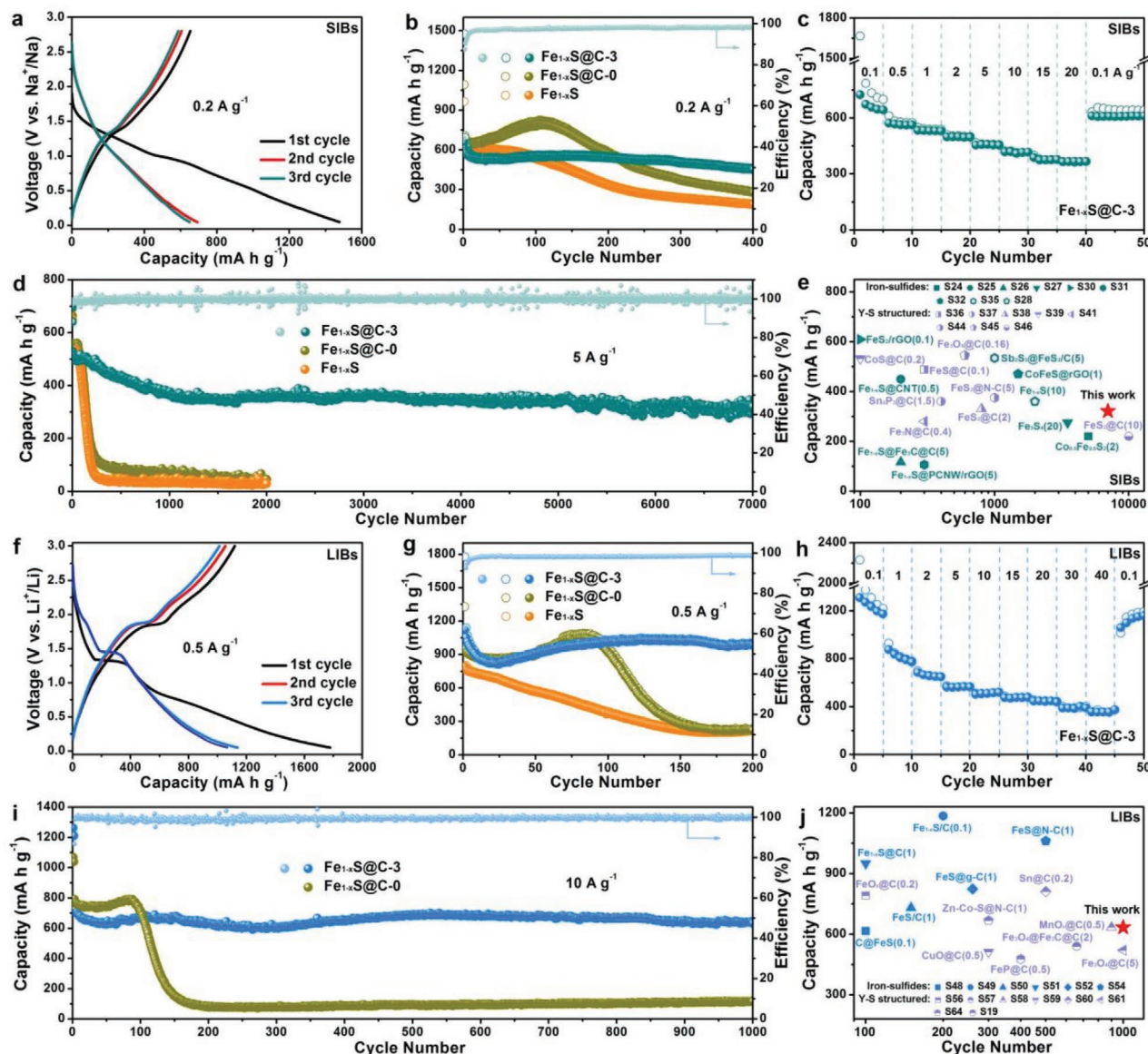**Figure 5.** a–e) Sodium and f–j) lithium storage performance of as-prepared composites. Initial three discharge/charge profiles of $Fe_{1-x}S@C-3$ at a) 0.2 A g^{-1} for SIBs and f) 0.5 A g^{-1} for LIBs. Cycling performance of $Fe_{1-x}S$, $Fe_{1-x}S@C-0$, and $Fe_{1-x}S@C-3$ electrodes at low current densities of b) 0.2 A g^{-1} for SIBs and g) 0.5 A g^{-1} for LIBs. Rate capability of $Fe_{1-x}S@C-3$ under various rates c) from 0.1 to 20 A g^{-1} for SIBs and h) from 0.1 to 40 A g^{-1} for LIBs. Long-term cycling performance of $Fe_{1-x}S$, $Fe_{1-x}S@C-0$, and $Fe_{1-x}S@C-3$ electrodes at high rates of d) 5 A g^{-1} for SIBs and i) 10 A g^{-1} for LIBs. Comparison of cycling performance between $Fe_{1-x}S@C-3$ and as-reported anodes for e) SIBs and j) LIBs.

Figure S24, Supporting Information from which the original nanosheet morphology was well reserved with active material NPs still encapsulated within hollow carbon shells. Based on the above results, the m-Y–S $Fe_{1-x}S@C-3$ composites, as anodes for LIBs, SIBs, and PIBs, exhibited high capacity, good rate capability, and ultra-stable cycling performance. Such battery performance is one of the best results for Y–S structures and iron sulfide-based anodes in the literature (Figure 5e,j and Tables S2, S4, S5, Supporting Information).

As a proof-of-concept, potassium ion full cells are further constructed by coupling $Fe_{1-x}S@C-3$ anode with perylenetetracarboxylic dianhydride (PTCDA) cathode.[73] As shown in Figure S25, Supporting Information, the annealed PTCDA

exhibited a stable capacity of 123 mA h g^{-1} at 0.1 A g^{-1} in half cells. The battery performance of PTCDA//$Fe_{1-x}S@C-3$ full cells was conducted between 0.5 and 3.0 V. In Figure S26, Supporting Information, full cells can deliver high discharge capacities around 330 mA h g^{-1} at 0.1 A g^{-1} as well as a rate capacity of 165 mA h g^{-1} at 1 A g^{-1} based on the mass of $Fe_{1-x}S@C-3$. Figure S26d, Supporting Information displays the cyclic behavior of full cell, which can sustain a capacity of 145 mA h g^{-1} after 150 cycles at 0.1 A g^{-1} and maintain high columbic efficiencies around 99% during cycles. Moreover, the PTCDA//$Fe_{1-x}S@C-3$ full cells can illuminate a light-emitting diode screen in Figure S27, Supporting Information, suggesting the potential application of $Fe_{1-x}S@C-3$ composite

in practical PIBs. Moreover, high-voltage cathodes (e.g., Prussian blue analogs, $KVPO_4F$) can be used to further enhance the average voltage and energy density of the full PIBs.[74,75]

3. Conclusion

In summary, we have developed a partial sulfuration strategy to construct m-Y–S structures with tunable internal void space. Compared with traditional Y–S structure, the structure merits of multiple contact points and small yolk size endowed m-Y–S $Fe_{1-x}S@C$-3 composite with outstanding battery performance for K/Na/Li-ion storage. As anode materials, it can present high reversible capacities and excellent rate capability (187 mA h g^{-1} at 10 A g^{-1} for K^+, 365 mA h g^{-1} at 20 A g^{-1} for Na^+, and 355 mA h g^{-1} at 40 A g^{-1} for Li^+). Notably, it delivered ultralong cycling stability up to 7000 and 20 000 cycles for SIBs and PIBs. Such extraordinary performance of $Fe_{1-x}S@C$-3 outperformed most reported anodes for Li/Na/K-ion storage. DFT calculations and kinetics analysis suggested the superior charge transportation ability of m-Y–S $Fe_{1-x}S@C$ than pure $Fe_{1-x}S$ and s-Y–S structure, thus benefiting for its ultra-stable cycling and superior rate capability. This work offers a new avenue to fabricate m-Y–S structures for achieving high-performance electrochemical energy storage.

4. Experimental Section

Synthesis of m-Y–S $Fe_{1-x}S@C$ Composites: Fe_2O_3 nanosheets were synthesized via a facile hydrothermal method. The carbon coating was realized by dispersing 80 mg Fe_2O_3 into 9.3 mL H_2O and sonicating for 0.5 h, followed with the addition of 0.024 mL $NH_3.H_2O$ and 0.3 mL 0.01 M cetyltrimethylammonium bromide aqueous solution. After being stirred for 0.5 h, 12 mg resorcinol and 0.0168 mL formaldehyde solution were added and stirred for another 16 h at room temperature. The product was filtered and washed with H_2O for several times, dried at 80 °C overnight, and further annealed at 550 °C for 2 h under Ar atmosphere, to obtain $Fe_3O_4@C$ composite.

During the partial sulfuration process, 100 mg $Fe_3O_4@C$ and a given amount of sulfur were sealed in a quartz tube under vacuum, followed with the sulfuration treatment at 300 °C for 6 h, and 400 °C for 3 h under a heating rate of 5 °C min^{-1}. Then, the obtained sample was taken out from the quartz tube, and further heated at 400 °C for 1 h under Ar. Next, as-obtained $Fe_3O_4/FeS_2@C$ composite was etched with 10 wt% HF solution for 1 h, and further annealed at 550 °C for 2 h, to achieve m-Y–S $Fe_{1-x}S@C$ composites. The composites prepared with different sulfur amounts of 40, 20, and 12 mg were denoted as $Fe_{1-x}S@C$-1, $Fe_{1-x}S@C$-2, and $Fe_{1-x}S@C$-3, respectively. $Fe_{1-x}S@C$-0 and bare $Fe_{1-x}S$ were synthesized by sulfuration treatment of $Fe_3O_4@C$ and Fe_2O_3 with excess sulfur (1:2 in weight), respectively, under the same procedure except without the HF etching.

Synthesis of s-Y–S $Fe_{1-x}S@C$ Composite: The s-Y–S structure sample was prepared through the acid-etching and subsequent sulfuration treatment. Typically, 80 mg above $Fe_3O_4@C$ sample was well dispersed in the mixture solution of 10 mL H_2O and 10 mL ethanol by sonicating for 1 h. Then, 20 mL 4 M HCl was added into the above solution and the reaction was kept for 6 h under mechanical stirring. The as-prepared s-Y–S $Fe_3O_4@C$ sample was mixed with sulfur power (1:2 in weight), sealed in a quartz tube under vacuum, and sulfurized at 400 °C for 3 h. The obtained sample was taken out, annealed at 400 °C for 1 h to evaporate excess sulfur, and further heated at 550 °C for 2 h to achieve s-Y–S $Fe_{1-x}S@C$ composite.

Materials Characterization: As-prepared composites were characterized through SEM (SU-8010), TEM (Tecnai F20), XRD (Shimadzu, Miniflex600), XPS (ESCALAB 250 Xi), and Brunauer–Emmett–Teller surface area analyzer (BET, Quantachrome Autosorb-iQ2-XR). The $Fe_{1-x}S$ contents in the composites were investigated via thermogravimetry analyses (TGA, NETZSCH STA449C) by heating in air atmosphere from 30 to 800 °C under a heating rate of 10 K min^{-1}.

Computational Methods: The present first-principle calculation was used to investigate the K ion properties in the structures based on DFT. The Perdew–Burke–Ernzerhof with projector-augmented wave had been employed in the calculation. It is noted that the $3 \times 3 \times 1$ K-points and 400 eV of cut-off energy was used to optimize the surface and interface structure. For the structure, the convergence criterion can be described as: the self-consistent force is less than 0.05 eV $Å^{-1}$ and the difference of energy is less than 10^{-6} eV. In addition, for the Fe atoms, the U schemes need to be applied, and the U has been set as 3.2 eV. What is more, K ions migration barrier energies had been evaluated using the climbing nudged elastic band methods. In the calculation, the adsorption energy can be obtained by the equation: $E_{ad} = E_{total} - E_1 - E_K$, where the E_{total} is the surface or interface structure with K ion adsorbed, E_1 is the energy of the surface or interface structure, E_K is the energy of K atoms.

Electrochemical Measurement: The electrochemical behavior of the samples was performed via CR2025 coin-type cells, which were assembled within an Ar-filled glove box (Mikrouna, universal 2440/750/900). To prepare working electrodes, $Fe_{1-x}S$-based composites, ketjen black, and carboxymethyl cellulose were mixed with a weight ratio of 70:15:15. After being grinding with certain amount of water for 30 min, as-obtained slurry was spread on Ni foam, and dried at 80 °C in a vacuum oven for 12 h. For LIBs, the counter electrode was lithium foil, and the separator was Celgard 2300 membrane. The electrolyte was 1 M $LiPF_6$ in ethylene carbonate (EC):dimethyl carbonate:ethylmethyl carbonate (1:1:1 in volume). For SIBs, sodium foil was used as the counter electrode, and the electrolyte was 1 M $NaClO_4$ in EC:diethyl carbonate (1:1 in volume) with 10 wt% fluoroethylene. For PIBs, potassium foil was the counter electrode, and the electrolyte was 0.5 M KPF_6 in EC:propylene carbonate (1:1 in volume). The separator was a glass fiber membrane (Whatman, GF/D) for both SIBs and PIBs. The mass loading per electrode was around 0.6–1.2 mg cm^{-2}. The amounts of electrolyte for LIBs, SIBs, and PIBs were around 40, 200, and 200 μL per coin cell, respectively.

The K-ion full cells were carried out through CR2025 coin cells by using $Fe_{1-x}S@C$-3 as the anode, PTCDA as the cathode, 3 M KFSI in DME as the electrolyte, and glass fiber membrane as the separator. The cathode was made by mixing thermally annealed PTCDA, super P carbon black, and carboxymethyl cellulose (8:1:1 in weight) with H_2O, which was then spread on Al foil. Prior to assembly the full cells, the PTCDA cathode was pre-cycled in half-cells at 0.1 A g^{-1} between 1.5 and 3.5 V, and the $Fe_{1-x}S@C$-3 anode was cycled in half cells for five cycles and then discharged to 0.05 V at 0.1 A g^{-1}. The capacity ratio of cathode to anode was controlled to be around 1.1:1. Before test, the full cell was initially discharged once at 0.1 A g^{-1}. The galvanostatic discharge/charge test was conducted on a battery tester (Land 2001A system) under various current densities from 0.1 to 20 A g^{-1}. The voltage ranges for half cells and full cells are 0.05–2.8 V and 0.5–3.0 V, respectively. Cyclic voltammetry was measured on a CHI660C electrochemical workstation from 0.2 to 2.0 mV s^{-1}. The specific capacity mentioned in the manuscript was calculated based on the whole mass of the $Fe_{1-x}S@C$ composites.

Supporting Information

Supporting Information is available from the Wiley Online Library or from the author.

Acknowledgements

[1] D. Larcher, J. M. Tarascon, *Nat. Chem.* **2015**, *7*, 19.
[2] C. P. Grey, J. M. Tarascon, *Nat. Mater.* **2017**, *16*, 45.
[3] Y. E. Durmus, H. Zhang, F. Baakes, G. Desmaizieres, H. Hayun, L. T. Yang, M. Kolek, V. Kupers, J. Janek, D. Mandler, S. Passerini, Y. Ein-Eli, *Adv. Energy Mater.* **2020**, *10*, 2000089.
[4] C. Delmas, *Adv. Energy Mater.* **2018**, *8*, 1703137.
[5] H. S. Hirsh, Y. X. Li, D. H. S. Tan, M. H. Zhang, E. Y. Zhao, Y. S. Meng, *Adv. Energy Mater.* **2020**, *10*, 2001274.
[6] R. Rajagopalan, Y. G. Tang, X. B. Ji, C. K. Jia, H. Y. Wang, *Adv. Funct. Mater.* **2020**, *30*, 1909486.
[7] T. Hosaka, K. Kubota, A. S. Hameed, S. Komaba, *Chem. Rev.* **2020**, *120*, 6358.
[8] L. Li, Y. Zheng, S. L. Zhang, J. P. Yang, Z. P. Shao, Z. P. Guo, *Energy Environ. Sci.* **2018**, *11*, 2310.
[9] Y. Y. Huang, Y. H. Zheng, X. Li, F. Adams, W. Luo, Y. H. Huang, L. B. Hu, *ACS Energy Lett.* **2018**, *3*, 1604.
[10] W. C. Zhang, Y. J. Liu, Z. P. Guo, *Sci. Adv.* **2019**, *5*, eaav7412.
[11] Y. X. Zhang, L. Zhang, T. A. Lv, P. K. Chu, K. F. Huo, *ChemSusChem* **2020**, *13*, 1114.
[12] Y. Z. Liu, C. H. Yang, Q. Y. Zhang, M. L. Liu, *Energy Stor. Mater.* **2019**, *22*, 66.
[13] Z. Hu, Q. N. Liu, S. L. Chou, S. X. Dou, *Adv. Mater.* **2017**, *29*, 1700606.
[14] H. T. Tan, Y. Z. Feng, X. H. Rui, Y. Yu, S. M. Huang, *Small Methods* **2020**, *4*, 1900563.
[15] S. H. Qi, B. L. Xu, V. T. Tiong, J. Hu, J. M. Ma, *Chem. Eng. J.* **2020**, *379*, 122261.
[16] M. Z. Chen, E. H. Wang, Q. N. Liu, X. D. Guo, W. H. Chen, S. L. Chou, S. X. Dou, *Energy Stor. Mater.* **2019**, *19*, 163.
[17] X. Li, S. H. Qi, W. C. Zhang, Y. Z. Feng, J. M. Ma, *Rare Met.* **2020**, *39*, 1239.
[18] E. Pomerantseva, F. Bonaccorso, X. L. Feng, Y. Cui, Y. Gogotsi, *Science* **2019**, *366*, eaan8285.
[19] J. W. Chen, D. H. C. Chua, P. S. Lee, *Small Methods* **2020**, *4*, 1900648.
[20] B. Chen, D. L. Chao, E. Z. Liu, M. Jaroniec, N. Q. Zhao, S. Z. Qiao, *Energy Environ. Sci.* **2020**, *13*, 1096.
[21] Y. Zhao, L. P. Wang, M. T. Sougrati, Z. X. Feng, Y. Leconte, A. Fisher, M. Srinivasan, Z. C. Xu, *Adv. Energy Mater.* **2017**, *7*, 1601424.
[22] Y. R. Liang, W. C. Zhang, D. C. Wu, Q. Q. Ni, M. Q. Zhang, *Adv. Mater. Interfaces* **2018**, *5*, 1800430.
[23] J. R. He, G. Hartmann, M. Lee, G. S. Hwang, Y. F. Chen, A. Manthiram, *Energy Environ. Sci.* **2019**, *12*, 344.
[24] H. Y. Geng, Y. Peng, L. T. Qu, H. J. Zhang, M. H. Wu, *Adv. Energy Mater.* **2020**, *10*, 1903030.
[25] Z. C. Zhao, Z. Q. Hu, R. S. Jiao, Z. H. Tang, P. Dong, Y. D. Li, S. D. Li, H. S. Li, *Energy Stor. Mater.* **2019**, *22*, 228.
[26] Q. H. Wang, C. Guo, Y. X. Zhu, J. P. He, H. Q. Wang, *Nano-Micro Lett.* **2018**, *10*, 30.
[27] Y. Liu, Y. J. Fang, Z. W. Zhao, C. Z. Yuan, X. W. Lou, *Adv. Energy Mater.* **2019**, *9*, 1803052.
[28] Y. Zhao, J. J. Zhu, S. J. H. Ong, Q. Q. Yao, X. L. Shi, K. Hou, Z. C. J. Xu, L. H. Guan, *Adv. Energy Mater.* **2018**, *8*, 1802565.
[29] Y. Xiao, J. Y. Hwang, I. Belharouak, Y. K. Sun, *ACS Energy Lett.* **2017**, *2*, 364.
[30] C. M. Chen, Y. C. Yang, X. Tang, R. H. Qiu, S. Y. Wang, G. Z. Cao, M. Zhang, *Small* **2019**, *15*, 1804740.
[31] K. Han, W. Zhao, Q. Y. Yu, Z. W. Liu, P. Li, W. Wang, L. Song, F. Q. An, P. Cao, X. H. Qu, *J. Power Sources* **2020**, *469*, 228429.
[32] C. Wu, X. Tong, Y. F. Ai, D. S. Liu, P. Yu, J. Wu, Z. M. M. Wang, *Nano-Micro Lett.* **2018**, *10*, 40.
[33] Q. Q. Yao, J. S. Zhang, J. X. Li, W. J. Huang, K. Hou, Y. Zhao, L. H. Guan, *J. Mater. Chem. A* **2019**, *7*, 18932.
[34] Z. M. Liu, T. C. Lu, T. Song, X. Y. Yu, X. W. Lou, U. Paik, *Energy Environ. Sci.* **2017**, *10*, 1576.
[35] J. R. He, L. Luo, Y. F. Chen, A. Manthiram, *Adv. Mater.* **2017**, *29*, 1702707.
[36] H. Yang, L.-W. Chen, F. He, J. Zhang, Y. Feng, L. Zhao, B. Wang, L. He, Q. Zhang, Y. Yu, *Nano Lett.* **2020**, *20*, 758.
[37] J. R. He, A. Manthiram, *Adv. Energy Mater.* **2020**, *10*, 2002654.
[38] Y. X. Wang, J. P. Yang, S. L. Chou, H. K. Liu, W. X. Zhang, D. Y. Zhao, S. X. Dou, *Nat. Commun.* **2015**, *6*, 8689.
[39] F. H. Yang, H. Goo, J. N. Hao, S. L. Zhang, P. Li, Y. Q. Liu, J. Chen, Z. P. Guo, *Adv. Funct. Mater.* **2019**, *29*, 1808291.
[40] Q. D. Li, L. Li, K. A. Owusu, W. Luo, Q. Y. An, Q. L. Wei, Q. J. Zhang, L. Q. Mai, *Nano Energy* **2017**, *41*, 109.
[41] Y. Y. Zhao, Q. Fu, D. S. Wang, Q. Pang, Y. Gao, A. Missiul, R. Nemausat, A. Sarapulova, H. Ehrenberg, Y. J. Wei, G. Chen, *Energy Stor. Mater.* **2019**, *18*, 51.
[42] X. Zhao, F. Y. Gong, Y. D. Zhao, B. Huang, D. Qian, H. E. Wang, W. H. Zhang, Z. J. Yang, *Chem. Eng. J.* **2020**, *392*, 123675.
[43] Y. Y. Liu, Y. Y. Zhu, Y. Cui, *Nat. Energy* **2019**, *4*, 540.
[44] B. Babu, P. Simon, A. Balducci, *Adv. Energy Mater.* **2020**, *10*, 2001128.
[45] Y. Zhao, X. L. Shi, S. J. H. Ong, Q. Q. Yao, B. B. Chen, K. Hou, C. T. Liu, Z. C. J. Xu, L. H. Guan, *ACS Nano* **2020**, *14*, 4463.
[46] L. Zhang, C. Wang, Y. Dou, N. Cheng, D. Cui, Y. Du, P. Liu, M. Al-Mamun, S. Zhang, H. Zhao, *Angew. Chem., Int. Ed.* **2019**, *58*, 8824.
[47] M. M. Chen, E. Y. Zhao, Q. B. Yan, Z. B. Hu, X. L. Xiao, D. F. Chen, *Sci. Rep.* **2016**, *6*, 29381.
[48] Y. Zhao, L. P. Wang, S. B. Xi, Y. H. Du, Q. Q. Yao, L. H. Guan, Z. C. J. Xu, *J. Mater. Chem. A* **2017**, *5*, 25609.
[49] W. Yang, X. L. Ma, X. W. Xu, Y. F. Li, S. I. Raj, G. Q. Ning, A. J. Wang, S. L. Chen, *J. Power Sources* **2015**, *282*, 228.
[50] G. K. Veerasubramani, Y. Subramanian, M. S. Park, G. Nagaraju, B. Senthilkumar, Y. S. Lee, D. W. Kim, *J. Mater. Chem. A* **2018**, *6*, 20056.
[51] X. X. Zhu, D. Liu, D. Zheng, G. W. Wang, X. K. Huang, J. S. Harris, D. Y. Qu, D. Y. Qu, *J. Mater. Chem. A* **2018**, *6*, 13294.
[52] D. Adekoya, H. Chen, H. Y. Hoh, T. Gould, M. S. J. T. Balogun, C. Lai, H. J. Zhao, S. Q. Zhang, *ACS Nano* **2020**, *14*, 5027.
[53] Q. Pan, F. Zheng, Y. Liu, Y. Li, W. Zhong, G. Chen, J. Hu, C. Yang, M. Liu, *J. Mater. Chem. A* **2019**, *7*, 20229.

**ADVANCED
SCIENCE NEWS**

www.advancedsciencenews.com

**ADVANCED
MATERIALS**

www.advmat.de

[54] H. Gao, T. F. Zhou, Y. Zheng, Q. Zhang, Y. Q. Liu, J. Chen, H. K. Liu, Z. P. Guo, *Adv. Funct. Mater.* **2017**, *27*, 1702634.

[55] S. P. Zhang, G. Wang, B. B. Wang, J. M. Wang, J. T. Bai, H. Wang, *Adv. Funct. Mater.* **2020**, *30*, 2001592.

[56] M. Z. Ma, S. P. Zhang, Y. Yao, H. Y. Wang, H. J. Huang, R. Xu, J. W. Wang, X. F. Zhou, W. J. Yang, Z. Q. Peng, X. J. Wu, Y. L. Hou, Y. Yu, *Adv. Mater.* **2020**, *32*, 2000958.

[57] Y. Zhao, J. X. Li, N. Wang, C. X. Wu, G. F. Dong, L. H. Guan, *J. Phys. Chem. C* **2012**, *116*, 18612.

[58] X. Li, H. P. Wang, W. C. Zhang, Y. Z. Feng, J. M. Ma, *Acta Metall. Sin. (Engl. Lett.)* **2021**, *34*, 321.

[59] Z. Liu, X. Y. Yu, U. Paik, *Adv. Energy Mater.* **2016**, *6*, 1502318.

[60] P. Jing, Q. Wang, B. Y. Wang, X. Gao, Y. Zhang, H. Wu, *Carbon* **2020**, *159*, 366.

[61] X. L. Shi, J. S. Zhang, Q. Q. Yao, R. Wang, H. F. Wu, Y. Zhao, L. H. Guan, *J. Mater. Chem. A* **2020**, *8*, 8002.

[62] D. L. Chao, C. R. Zhu, P. H. Yang, X. H. Xia, J. L. Liu, J. Wang, X. F. Fan, S. V. Savilov, J. Y. Lin, H. J. Fan, Z. X. Shen, *Nat. Commun.* **2016**, *7*, 12122.

[63] Q. Q. Yao, J. S. Zhang, X. L. Shi, B. L. Deng, K. Hou, Y. Zhao, L. H. Guan, *Electrochim. Acta* **2019**, *307*, 118.

[64] L. Yang, W. W. Hong, Y. Zhang, Y. Tian, X. Gao, Y. R. Zhu, G. Q. Zou, H. S. Hou, X. B. Ji, *Adv. Funct. Mater.* **2019**, *29*, 1903454.

[65] Y. Xu, C. L. Zhang, M. Zhou, Q. Fu, C. X. Zhao, M. H. Wu, Y. Lei, *Nat. Commun.* **2018**, *9*, 1720.

[66] Y. H. Zou, Y. Gu, B. Hui, X. F. Yang, H. W. Liu, S. Chen, R. S. Cai, J. Sun, X. L. Zhang, D. J. Yang, *Adv. Energy Mater.* **2020**, *10*, 1904147.

[67] Y. Liu, Z. H. Sun, X. Sun, Y. Lin, K. Tan, J. F. Sun, L. W. Liang, L. R. Hou, C. Z. Yuan, *Angew. Chem., Int. Ed.* **2020**, *59*, 2473.

[68] Y. X. Tang, Y. Y. Zhang, W. L. Li, B. Ma, X. D. Chen, *Chem. Soc. Rev.* **2015**, *44*, 5926.

[69] J. H. Chu, W. A. Wang, J. R. Feng, C. Y. Lao, K. Xi, L. D. Xing, K. Han, Q. Li, L. Song, P. Li, X. Li, Y. P. Bao, *ACS Nano* **2019**, *13*, 6906.

[70] B. Chen, H. Li, H. X. Liu, X. Q. Wang, F. X. Xie, Y. D. Deng, W. B. Hu, K. Davey, N. Q. Zhao, S. Z. Qiao, *Adv. Energy Mater.* **2019**, *9*, 1901146.

[71] J. C. Guo, Q. Liu, C. S. Wang, M. R. Zachariah, *Adv. Funct. Mater.* **2012**, *22*, 803.

[72] D. P. Li, Y. M. Zhang, Q. Sun, S. N. Zhang, Z. P. Wang, Z. Liang, P. C. Si, L. J. Ci, *Energy Stor. Mater.* **2019**, *23*, 367.

[73] J. Wang, L. Fan, Z. M. Liu, S. H. Chen, Q. F. Zhang, L. L. Wang, H. G. Yang, X. Z. Yu, B. A. Lu, *ACS Nano* **2019**, *13*, 3703.

[74] M. Fiore, S. Wheeler, K. Hurlbutt, I. Capone, J. Fawdon, R. Ruffo, M. Pasta, *Chem. Mater.* **2020**, *32*, 7653.

[75] H. Kim, D. H. Seo, M. Bianchini, R. J. Clement, H. Kim, J. C. Kim, Y. S. Tian, T. Shi, W. S. Yoon, G. Ceder, *Adv. Energy Mater.* **2018**, *8*, 1801591.

2100837 (12 of 12)